Advanced modelling of microgel structure across the volume phase transition

Andrea Ninarello[1,2], Jérôme J. Crassous[3,4],[a] Divya Paloli[4], Fabrizio Camerin[1,5], Nicoletta Gnan[1,2], Lorenzo Rovigatti[2,1], Peter Schurtenberger[4], and Emanuela Zaccarelli[1,2b]

[1] *CNR-ISC Uos Sapienza, Piazzale A. Moro 2, IT-00185 Roma, Italy*

[2] *Department of Physics,* Sapienza *Università di Roma, Piazzale A. Moro 2, IT-00185 Roma, Italy*

[3] *Institute of Physical Chemistry, RWTH Aachen University, Landoltweg 2, DE-52074 Aachen, Germany*

[4] *Physical Chemistry, Department of Chemistry, Lund University, Naturvetarvägen 14, SE-22100 Lund, Sweden and*

[5] *Department of Basic and Applied Sciences for Engineering,* Sapienza *Università di Roma, via A. Scarpa 14, IT-00161 Roma, Italy*

(Dated: February 1, 2019)

Thermoresponsive microgels are soft colloids that find widespread use as model systems for soft matter physics. Their complex internal architecture, made of a disordered and heterogenous polymer network, has been so far a major challenge for computer simulations. In this work we introduce an advanced coarse-grained model of microgels whose structural properties are in quantitative agreement with results obtained with small-angle X-ray scattering experiments across a wide range of temperatures, encompassing the volume phase transition. These results bridge the gap between experiments and simulations of individual microgel particles, paving the way to theoretically address open questions about their bulk properties with unprecedented microscopic resolution.

As many fields of physics, colloidal science has profoundly benefited from the interplay between experiments and computer simulations. In the last decades, the epitome of colloids in suspension was represented by Poly(methyl methacrylate) (PMMA) particles in experiments [1] and by their numerical analogous, the hard sphere model [2]. However, in more recent years, colloids with internal degrees of freedom and tunable softness have been progressively replacing hard spheres in experimental studies [3]. Among these, microgels, i.e. spherical particles made of a crosslinked polymer network, have become particularly popular among physicists [4] for two main reasons: (i) a relatively easy synthesis protocol yielding quite monodisperse particles and (ii) the possibility of finely tuning the particle properties by changing the chemical composition of the constituent polymers. For example, in the case of thermoresponsive polymers such as Poly(N-isopropylacrylamide) (PNIPAM), microgels undergo a so-called Volume Phase Transition (VPT) at a temperature $T_{VPT} \sim 32°$C across which they change from a swollen state at low temperatures to a compact state at high temperatures. Due to their high versatility, microgels have been used to address numerous open problems in statistical physics, including the jamming transition at finite temperature [5], premelting within crystalline states [6], geometric frustation in colloids [7], depletion effects [8, 9], nucleation of squeezable particles [10–12] and the glass transition of soft colloids [13–15].

The downside of using PNIPAM microgels, which are usually synthesized with radical emulsion or precipitation polymerization, is an incomplete control on the internal particle topology [16], usually comprising a dense core and an outer corona, which is rather heterogenous and mainly composed of long chains and few crosslinkers [4]. One of the most successful descriptions of the internal topology of microgels is the so-called fuzzy sphere model, in which a strictly homogeneous core is surrounded by a looser corona [17]. The use of super-resolution microscopy[18–20] recently allowed the real space visualization of the internal density profiles of the microgels, revealing that the core is not really homogeneous, being denser in its inner part and progressively rarifying towards the corona [21, 22].

In order to go beyond simple pair-wise potentials such as Hertzian or harmonic ones [14, 15, 23], which completely neglect the internal degrees of freedom of microgels, few attempts to model the polymeric aspects of individual microgels in simulations have been recently put forward [24]. While early works were mostly relying on the use of a polymeric crystalline network [25–28], a few papers later reported the *in silico* realization of disordered crosslinked networks [29–31]. However, all the methods proposed so far were unable to finely control the internal density distribution of the network and, consequently, to reproduce the properties of the experimentally available microgels in a truly quantitative fashion.To this aim, it is also important to assess the role played by the coarse-grained level of description, and thus of the system size, on the final result.

In this Letter, we put forward a novel numerical methodology where microgels with desired internal density profiles are generated. Building on the assembly protocol proposed in Ref. [30], we introduce a designing force on the crosslinkers that is able to tune the core-corona relative extent independently of the system size. By carefully adjusting the force field and intensity, we obtain individual microgel particles that quantitatively reproduce the experimentally measured form factors and swelling behavior across the VPT. We also quantify the effect of

[a] crassous@pc.rwth-aachen.de

[b] emanuela.zaccarelli@cnr.it

the coarse-graining on the structure of the *in silico* microgels by performing our investigation as a function of simulated system size. Our results close the gap between numerical and experimental investigation of microgels, paving the way to a deeper theoretical understanding of these soft colloids.

We perform two different kinds of simulations. Initially, we generate microgels with crosslinker concentration $c = 5\%$ through the self-assembly of patchy particles [30] confined within a spherical cavity. Particles with two and four patches, representing monomers and crosslinkers respectively, interact via the sum of a Weeks-Chandler-Andersen (WCA) repulsion [32] and an attractive patchy potential [33]. We perform simulations with $N = 5000, 42000, 336000$ beads of unit mass m in cavities respectively of diameter $Z = 25, 50, 100$ in units of bead size σ in order to maintain the final number density of the microgel roughly constant. In order to accelerate the network formation, we employ a bond-swapping algorithm [34]. With the aim of controlling the final density distribution and the width of the corona, we introduce a designing force which pulls crosslinkers towards the cavity centre. This force is made of two contributions: (i) an elastic force of spring constant k acting from the center of the cavity up to a distance $\frac{Z}{2}$ and (ii) a gravity-like force of strength g being at work between $\frac{Z}{2}$ and Z. An illustration of the resulting microgel and of the designing force is reported in Fig. 1, while detailed information about the choice of the form and intensity of the force is provided in the SI. We perform NVT molecular dynamics simulations with an Andersen thermostat at temperature $T^* = \frac{k_B T}{\epsilon} = 0.03$, where ϵ is the energy unit of the WCA potential (see SI), until at least $\gtrsim 99.9\%$ of the particles are connected into a single network. Thereafter, we replace the patchy potential with a bead-spring interaction [35], where the repulsive WCA potential is complemented by a spring-like Finitely Extensible Nonlinear Elastic (FENE) potential between connected monomers. This model correctly implements the connectivity properties of polymers and preserves the topology of the network throughout the rest of the simulations. Finally, we discard the particles that are not connected to the main cluster and obtain the assembled microgel configurations. This procedure is repeated for ten independent configurations for each investigated system size, in order to averaging over different network realizations.

Once the network is built, we perform Nose-Hoover molecular dynamics runs with the LAMMPS package [36] at fixed temperature $T^* = 1$ with a time step $\delta t = 0.002$. The microgel is at first equilibrated for 1×10^6 time steps until its radius of gyration R_g reaches a constant value. After equilibration, a production run is performed for up to 1×10^7 time steps, saving configurations every 5×10^5 steps. From these, we calculate the form factor of the microgel, defined as

$$P(q) = \frac{1}{N} \sum_{ij} \langle \exp(-i\vec{q} \cdot \vec{r}_{ij}) \rangle, \qquad (1)$$

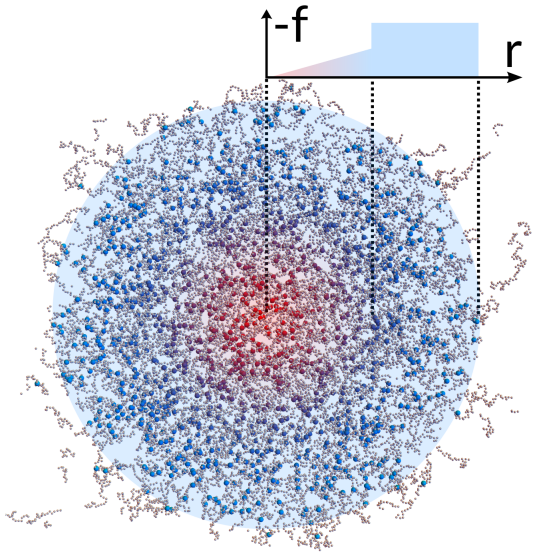

FIG. 1. Snapshot of a $N \approx 336000$ microgel slice of width 20σ. Monomers are represented in grey, while crosslinkers (magnified in size with respect to monomers to improve visualization) are coloured from red in the center to blue in the corona, following the shape of the designing force of magnitude f, which is illustrated in the top right corner. The use of the force correctly imposes an inhomogeneous profile to the microgel, with a larger concentration of crosslinkers in the core region. At the microgel boundary, few chains are disconnected since in this representation parts of the corona are outside the field of view.

where the angular brackets indicate an average over the equilibrium configurations, q is the wave vector and r_{ij} is the distance between monomers i and j. We also evaluate the radial density profile $\rho(r)$ as a function of the distance r from the center of mass of the microgel. The two observables $\rho(r)$ and $P(q)$ allow to compare the structure of the *in silico* microgels with experiments both in real and in reciprocal space. To mimic the thermoresponsive nature of microgels, we introduce an additional attractive potential between monomers, V_α [30, 37, 38], that takes into account the monomer-solvent interactions in an implicit way. The attraction strength between monomers is controlled by the solvophobic parameter α, which plays the role of an effective temperature. Further details on the model can be found in the SI.

Experiments were performed on microgels with $c = 5\%$ synthesized by precipitation polymerization as described in previous studies [14, 23]. Small angle X-ray scattering (SAXS) measurements of the microgel form factors were carried out at the Swiss Light Source (SLS, Paul Scherrer Institute) and their swelling behavior was characterized by dynamic light scattering (DLS). Further details on the experimental methods are provided in the SI.

The comparison between simulation and experimental results is represented in Fig. 2(a) that shows the form factors $P(q)$ measured by SAXS at different temperatures

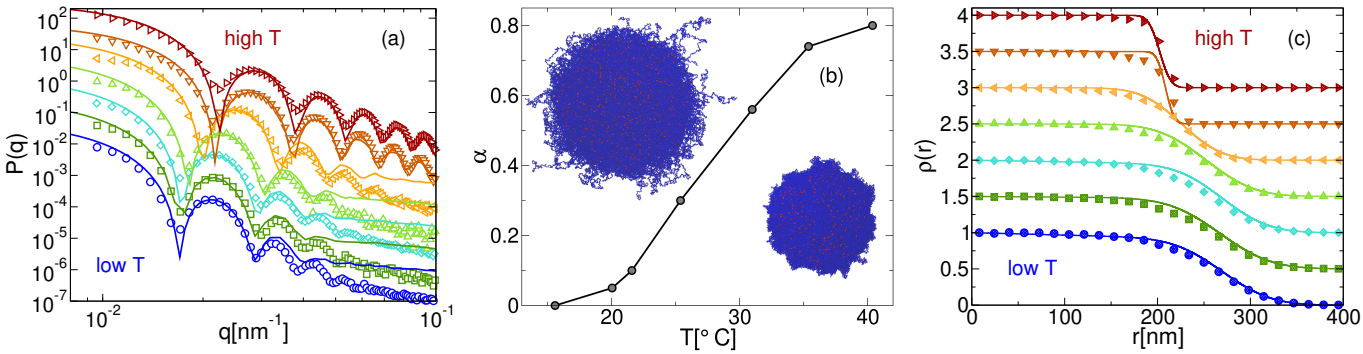

FIG. 2. (a) Comparison between experimental (empty symbols) and numerical (Eq. (1), full lines) form factors for $N \approx 336000$. The x-axis is rescaled by $\gamma = q^*_{\rm exp}/q^*_{\rm sim} = 0.2326$, where q^* is the position of the first peak of $P(q)$. Different colors correspond to different temperatures T and solvophobic parameters α, increasing from bottom to top: T = 15.6, 20.1, 21.6, 25.4, 31.0, 35.4, 40.4 °C in experiments and α = 0.00, 0.05, 0.10, 0.30, 0.56, 0.74, 0.80 in simulations. Data at different T, α are arbitrarily rescaled on the y-axis to help visualization; (b) mapping between T and α. The two snapshots show microgels with $N \approx 336000$ in swollen (top left) and collapsed (bottom right) conditions with monomers in blue and crosslinkers in red; (c) comparison between numerical (full symbols) and experimental (full lines) density profiles $\rho(r)$, where the latter are obtained by fitting the form factors to the generalized fuzzy sphere model (Eq. (2)). The numerical x-axis is rescaled by γ^{-1}, while data are normalized to 1 at the center of the microgel and shifted vertically by 0.5 at different T to improve readability.

and those calculated in the simulations. Up to the third peak, the agreement between experiments and simulations is remarkably good at all T. Both the positions and the shapes of the peaks are reproduced by the numerical data. At high T, where the microgel collapses and becomes more homogeneous, the agreement improves even further, with the numerical data being able to capture the positions and heights of all measured peaks. We notice that the deviations occurring at large q are entirely attributable to the smaller size of the numerical microgels as compared to the laboratory ones, leading to a different short lengthscale structure and scaling behaviour, as discussed in the following.

The comparison in Fig. 2(a) is performed by scaling the first peak position $q^*_{\rm sim}$ of the numerical $P(q)$ onto that of the experiments $q^*_{\rm exp}$ at the lowest available temperature ($T = 15.6°C$), which we set as the maximally swollen case in our model ($\alpha = 0$). This procedure defines a single scaling factor $\gamma = q^*_{\rm exp}/q^*_{\rm sim}$ that allows to convert numerical units into real ones and that is kept constant, regardless of the temperature. We next adjust the value of the solvophobic interaction strength α in order to capture the T-variation of $P(q)$. The resulting relationship between α and T is illustrated in Fig. 2(b). We find that a purely linear dependence holds at intermediate temperatures, showing some deviations at low and high T. While the former may be due to the arbitrary choice of the $\alpha = 0$ value with the lowest available T, the latter is more likely related to the implicit nature of the solvent employed in the simulations. We note in passing that this is the first direct test of the V_α potential against experiments across the VPT.

In order to directly visualize the internal structure of the system, we move to real space. To obtain the experimental radial density distributions from the scattering data, we need to fit the measured form factors. Building on the evidence from recent super-resolution microscopy experiments [21], we employ an extended fuzzy sphere model (detailed in the SI), which includes the possibility of a linear dependence of the density profile within the core. In real space, this can be written as:

$$\rho(r) \propto \mathrm{Erfc}\left[\frac{r - R'}{\sqrt{2}\sigma_{\rm surf}}\right](1 - sr), \qquad (2)$$

where R' corresponds to the radius at which the profile has decreased to half the core density, $\sigma_{\rm surf}$ quantifies the width of the corona and s is the slope of the linear decay inside the core. Values of the latter parameter are found to be always rather small, $s < 5 \times 10^{-4} nm^{-1}$. We also calculate $\rho(r)$ directly from simulations, which are mapped back to real units by rescaling the x-axis by $1/\gamma$. The comparison between numerical and experimental data is reported in Fig. 2(c) for all studied temperatures. The agreement is again found to be very good throughout the whole T range for both the core and the corona regions. We stress that the use of the standard fuzzy sphere model with a homogeneous core to fit the experimental $P(q)$ not only is at odds with super-resolution data [21], but it also yields density profiles that are in worse agreement with numerical data, as discussed in the SI. Interestingly, we find small but finite values of $\sigma_{\rm surf}$ also above the VPT, which is consistent with the fact that, even in the collapsed state, the microgels still contain a large amount of water [39]. This is confirmed by the snapshots shown in Fig. 2(b), where many dangling ends are clearly visible in the swollen state, giving rise to a rough profile of the microgel also in the collapsed state.

It is now important to comment on the robustness of our results with respect to system size. Of course, the use of a large number of monomers provides a remarkable improvement in the quantitative comparison with experiments, at the cost of a huge increase of the required

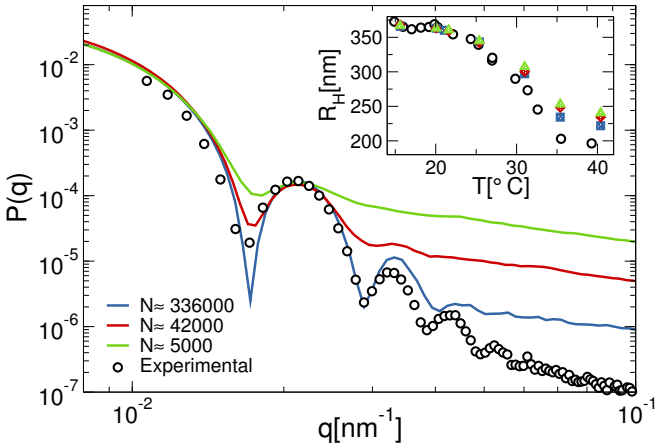

FIG. 3. Experimental (black circles) and simulation (full lines) form factors $P(q)$ in the swollen state. Numerical results comprise three system sizes obtained with the same designing force: $N \approx 336000$ (blue line), $N \approx 42000$ (red line), $N \approx 5000$ (green line). We employ the rescale factors $\gamma_{42000} = 0.1245$ and $\gamma_{5000} = 0.05798$. Inset: hydrodynamic radius R_H from experiments (black circles) and simulations (see text for its definition) for $N \approx 336000$ (blue squares), $N \approx 42000$ (red diamonds), $N \approx 5000$ (green triangles), respectively. Numerical data are rescaled to match experiments at low T.

computational resources. This is evident in Fig. 3, where $P(q)$ in the swollen state is calculated for three different system sizes and compared to experiments. In all cases, the first peaks of the numerical $P(q)$ have been rescaled to the experimental result, re-defining the unit length of the simulations. We observe that the first peak of the smallest system ($N \approx 5000$) is just barely visible. The peak becomes more well-defined by increasing the microgel radius by a factor of ~ 2 ($N \approx 42000$), with the simultaneous appearance of a second peak. Finally the largest system ($N \approx 336000$), corresponding to a further increase by a factor of ~ 2 in radius, reproduces quite well three out of the four peaks observed in the experimental curve. For all sizes, the relative distance of the peaks is maintained, but upon increasing N the high-q decay of $P(q)$ shifts down, in closer agreement to experiments. Thus, size effects alone can explain the high-q deviations observed in Fig. 2(a) between experiments and simulations. Importantly, we find that the relationship between T and α, shown in Fig. 2(b) is unaffected by size effects (see also SI). Interestingly, the numerical form factors at large wave-vectors can be well-described by an inverse power law, $P(q) \approx q^{-n}$, with $n \sim 1$ for all investigated cases. The fact that n does not vary with system size confirms that microgels with different N possess the same topological structure, at least on a mesoscopic scale. Consequently, the system size becomes a parameter that can be optimised in order to reproduce the properties of interest while, at the same time, reducing the computational effort.

However, size effects may still play a role in the ability of simulations to reproduce the experimental swelling ratio. This is the most used observable to quantify the VPT of microgels, because it can be readily obtained by DLS. The measured hydrodynamic radius R_H is reported in the inset of Fig. 3 and compared to the numerical analogous quantity, that is defined as the distance at which $\rho(R_H) = 10^{-3}$[30]. While both experimental and numerical R_H display a sharp size change with increasing temperature, we find that in simulations the collapse is less pronounced when the system size is reduced. This may be due to steric effects of the bead size in the collapsed state, which are more important for small microgels. However, we infer from the present study that in order to reach a realistic value of the PNIPAM monomer size $\sigma \sim 1nm$, we should increase the number of beads up to $N \approx 2 \times 10^7$, which is unfeasible with present day computational techniques. We further notice that charge effects, which become relevant above the VPT temperature [40], should be taken into account for a more faithful representation of the behavior of the numerical R_H at high T.

In conclusion, in this work we have shown how computer simulations can realistically model thermoresponsive microgels by adopting a designing force during the network assembly which can be tuned to quantitatively reproduce experimental form factors for a wide range of temperatures across the VPT. Even if the protocol itself is far from realistic and does not reproduce the experimental conditions of the synthesis, it is able to generate networks with arbitrary topologies that can closely match experimental data. We have shown that the protocol is robust to system size and reproduces very well the experimental form factors, including high-order peaks for very large microgels. It is worthwhile noting that the comparison is good even for microgels composed by a few thousands monomers, which can be routinely studied in simulations. This allows us to establish a relationship between the solvophobic strength α used in simulations and the experimental temperature T, finding that they are linearly related across the VPT, as expected. Our results reconcile experimental and numerical investigations, opening the possibility to address numerous questions about microgels, both at the fundamental and applicative level. The next step will be to make use of the knowledge gained at the single-particle level to develop models able to describe bulk suspensions of microgels [33]. Additionally, the protocol developed here is very general, making it possible to use it to tackle the investigation of the structure and behaviour of microgels with different density profiles, including homogeneous[41], hollow [42, 43] and ultrasoft ones [44–46], nowadays synthesized in experiments.

I. ACKNOWLEDGMENTS

We thank M. Paciolla for early contributions to this work. AN, FC, NG, LR and EZ acknowledge financial

support from the European Research Council (ERC Consolidator Grant 681597, MIMIC). PS acknowledges financial support from the European Research Council (ERC-339678-COMPASS) and the Swedish Research Council (VR 2015-05426). JJC thanks the German Research Foundation (Collaborative Research Center SFB985). SAXS experiments were performed at the cSAXS beam line of the Swiss Light Source SLS at Paul Scherrer Institute, and we gratefully acknowledge the help of the local contact A. Menzel.

[1] P. Bartlett and W. van Megen, "Physics of hard-sphere colloidal suspensions," in *Granular Matter: An Interdisciplinary Approach*, edited by A. Mehta (Springer New York, New York, NY, 1994) pp. 195–257.
[2] D. Frenkel and B. Smit, *Understanding Molecular Simulation: From Algorithms to Applications (Computational Science Series, Vol 1)* (Academic Press, 2001).
[3] D. Vlassopoulos and M. Cloitre, Current opinion in colloid & interface science **19**, 561 (2014).
[4] A. Fernandez-Nieves, H. M. Wyss, J. Mattsson, and D. A. Weitz, *Microgel Suspensions: Fundamentals and Applications* (Wiley-VCH, 2011).
[5] Z. Zhang, N. Xu, D. T. N. Chen, P. Yunker, A. M. Alsayed, K. B. Aptowicz, P. Habdas, A. J. Liu, S. R. Nagel, and A. G. Yodh, Nature **459**, 230 (2009).
[6] A. M. Alsayed, Science **309**, 1207 (2005).
[7] Y. Han, Y. Shokef, A. M. Alsayed, P. Yunker, T. C. Lubensky, and A. G. Yodh, Nature **456**, 898 (2008).
[8] C. Zhao, G. Yuan, D. Jia, and C. C. Han, Soft Matter **8**, 7036 (2012).
[9] M. J. Bergman, N. Gnan, M. Obiols-Rabasa, J.-M. Meijer, L. Rovigatti, E. Zaccarelli, and P. Schurtenberger, Nature Communications (2018), 10.1038/s41467-018-07332-5.
[10] A. S. Iyer and L. Lyon, Angewandte Chemie International Edition **48**, 4562 (2009).
[11] D. Frenkel, Nature **460**, 465 (2009).
[12] A. Scotti, U. Gasser, E. S. Herman, M. Pelaez-Fernandez, J. Han, A. Menzel, L. A. Lyon, and A. Fernández-Nieves, Proceedings of the National Academy of Sciences **113**, 5576 (2016).
[13] J. Mattsson, H. M. Wyss, A. Fernandez-Nieves, K. Miyazaki, Z. Hu, D. R. Reichman, and D. A. Weitz, Nature **462**, 83 (2009).
[14] D. Paloli, P. S. Mohanty, J. J. Crassous, E. Zaccarelli, and P. Schurtenberger, Soft Matter **9**, 3000 (2013).
[15] A.-M. Philippe, D. Truzzolillo, J. Galvan-Myoshi, P. Dieudonné-George, V. Trappe, L. Berthier, and L. Cipelletti, Physical Review E **97** (2018), 10.1103/physreve.97.040601.
[16] L. A. Lyon and A. Fernandez-Nieves, Annual Review of Physical Chemistry **63**, 25 (2012).
[17] M. Stieger, W. Richtering, J. S. Pedersen, and P. Lindner, The Journal of Chemical Physics **120**, 6197 (2004).
[18] G. M. Conley, S. Nöjd, M. Braibanti, P. Schurtenberger, and F. Scheffold, Colloids and Surfaces A: Physicochemical and Engineering Aspects **499**, 18 (2016).
[19] A. P. H. Gelissen, A. Oppermann, T. Caumanns, P. Hebbeker, S. K. Turnhoff, R. Tiwari, S. Eisold, U. Simon, Y. Lu, J. Mayer, W. Richtering, A. Walther, and D. Wöll, Nano Letters **16**, 7295 (2016).
[20] G. M. Conley, P. Aebischer, S. Nöjd, P. Schurtenberger, and F. Scheffold, Science Advances **3**, e1700969 (2017).
[21] S. Bergmann, O. Wrede, T. Huser, and T. Hellweg, Physical Chemistry Chemical Physics **20**, 5074 (2018).
[22] E. Siemes, O. Nevskyi, D. Sysoiev, S. K. Turnhoff, A. Oppermann, T. Huhn, W. Richtering, and D. Wöll, Angewandte Chemie International Edition **57**, 12280 (2018).
[23] P. S. Mohanty, D. Paloli, J. J. Crassous, E. Zaccarelli, and P. Schurtenberger, The Journal of Chemical Physics **140**, 094901 (2014).
[24] L. Rovigatti, N. Gnan, L. Tavagnacco, A. J. Moreno, and E. Zaccarelli, Soft Matter (2019), 10.1039/c8sm02089b.
[25] F. A. Escobedo and J. J. de Pablo, Physics Reports **318**, 85 (1999).
[26] P. K. Jha, J. W. Zwanikken, F. A. Detcheverry, J. J. de Pablo, and M. O. de la Cruz, Soft Matter **7**, 5965 (2011).
[27] H. Kobayashi and R. Winkler, Polymers **6**, 1602 (2014).
[28] S. Ahualli, A. Martín-Molina, J. A. Maroto-Centeno, and M. Quesada-Pérez, Macromolecules **(5)**, 2229 (2017).
[29] S. Nikolov, A. Fernandez-Nieves, and A. Alexeev, Applied Mathematics and Mechanics **39**, 47 (2017).
[30] N. Gnan, L. Rovigatti, M. Bergman, and E. Zaccarelli, Macromolecules **50**, 8777 (2017).
[31] A. J. Moreno and F. L. Verso, Soft Matter **14**, 7083 (2018).
[32] J. D. Weeks, D. Chandler, and H. C. Andersen, The Journal of Chemical Physics **54**, 5237 (1971).
[33] L. Rovigatti, G. Nava, T. Bellini, and F. Sciortino, Macromolecules **51**, 1232 (2018).
[34] F. Sciortino, The European Physical Journal E **40** (2017), 10.1140/epje/i2017-11496-5.
[35] K. Kremer and G. S. Grest, The Journal of Chemical Physics **92**, 5057 (1990).
[36] S. Plimpton, Journal of Computational Physics **117**, 1 (1995).
[37] T. Soddemann, B. Dünweg, and K. Kremer, The European Physical Journal E **6**, 409 (2001).
[38] F. L. Verso, J. A. Pomposo, J. Colmenero, and A. J. Moreno, Soft Matter **11**, 1369 (2015).
[39] I. Bischofberger and V. Trappe, Scientific Reports **5** (2015), 10.1038/srep15520.
[40] D. Truzzolillo, S. Sennato, S. Sarti, S. Casciardi, C. Bazzoni, and F. Bordi, Soft Matter **14**, 4110 (2018).
[41] E. Mueller, R. J. Alsop, A. Scotti, M. Bleuel, M. C. Rheinstädter, W. Richtering, and T. Hoare, Langmuir **34**, 1601 (2018).
[42] S. Nayak, D. Gan, M. Serpe, and L. Lyon, Small **1**, 416 (2005).
[43] A. Scotti, M. Brugnoni, A. A. Rudov, J. E. Houston, I. I. Potemkin, and W. Richtering, The Journal of Chemical Physics **148**, 174903 (2018).
[44] J. Gao and B. J. Frisken, Langmuir **19**, 5212 (2003).
[45] H. Bachman, A. C. Brown, K. C. Clarke, K. S. Dhada, A. Douglas, C. E. Hansen, E. Herman, J. S. Hy-

att, P. Kodlekere, Z. Meng, S. Saxena, M. W. S. Jr, N. Welsch, and L. A. Lyon, Soft Matter **11**, 2018 (2015).
[46] O. L. J. Virtanen, A. Mourran, P. T. Pinard, and W. Richtering, Soft Matter **12**, 3919 (2016).

Supplemental Material for Advanced modelling of microgel structure across the volume phase transition

Andrea Ninarello[1,2], Jérôme J. Crassous[3,4],[a] Divya Paloli[4], Fabrizio Camerin[1,5], Nicoletta Gnan[1,2], Lorenzo Rovigatti[2,1], Peter Schurtenberger[4], and Emanuela Zaccarelli[1,2b]

[1] *CNR-ISC Uos Sapienza, Piazzale A. Moro 2, IT-00185 Roma, Italy*

[2] *Department of Physics,* Sapienza *Università di Roma, Piazzale A. Moro 2, IT-00185 Roma, Italy*

[3] *Institute of Physical Chemistry, RWTH Aachen University, Landoltweg 2, DE-52074 Aachen, Germany*

[4] *Physical Chemistry, Department of Chemistry, Lund University, Naturvetarvägen 14, SE-22100 Lund, Sweden and*

[5] *Department of Basic and Applied Sciences for Engineering,* Sapienza *Università di Roma, via A. Scarpa 14, IT-00161 Roma, Italy*

(Dated: February 1, 2019)

I. DETAILS ON MICROGEL SYNTHESIS AND CHARACTERIZATION

A. Synthesis

PNIPAM microgels were synthesized by surfactant free radical polymerization as described in former studies [1, 2]. NIPAM (2 g) as monomers, N,N'-methylenebisacrylamide (BIS, 0.136 g) as cross-linker, and methacryloxyethyl thiocarbomoyl rhodamine B (2 mg dissolved in 87.8 mL of water) as the dye were polymerized by precipitation polymerization. The reaction was initiated by dropwised addition of sodium dodecylpersulfate initiator (0.01 g in 10 mL of water) at 80 °C and run for 4 h under constant stirring at 300 rpm and nitrogen purging. The reaction mixture was passed through glass wool in order to remove particulate matter. The dispersions was purified by repeated centrifugation/redispersion cycles against an aqueous 10^{-3} M potassium chloride (KCl) solution. The different suspensions were further obtained by dilution of the stock suspension with the aqueous KCl solution.

B. Small angle X-ray scattering (SAXS)

Experiments were performed at the Swiss Light Source (SLS, Paul Scherrer Institute) at the cSAXS instrument. A X-ray beam with an energy of 11.2 keV was used, corresponding to a wavelength $\lambda = 0.111$ nm. The q-scale was calibrated by a measurement of silver behenate. No absolute calibration was done for the X-ray data. The sample consists of a 1 wt% microgel dispersion containing 10^3 M KCl enclosed in a 1 mm diameter sealed quartz capillaries (Hilgenberg GmbH, Malsfeld, Germany) placed in a homemade thermostated aluminum sample holder ensuring a temperature control with an accuracy of 0.2 °C. At least 30 2D images were taken, azimuthally integrated, transmission and background corrected, and averaged according to established procedures provided by PSI.

C. Dynamic light scattering (DLS)

Experiments were carried out using a light scattering goniometer instrument from LS Instruments equipped with a HeNe laser light source with a wavelength $\lambda = 632.8nm$ and a maximum power of 35 mW. The sample is filled into cylindrical NMR tube of a diameter of 5 mm and placed in the temperature controlled index matching bath (±0.1 °C). The scattered light is detected by two APD detectors and processed by a Flex correlator in cross-correlation configuration. A modulation unit was employed as recently described by Block et al. [3] All the measurements were performed on a aqueous 0.01 wt% suspension containing 10^{-3} M KCl. The scattering angle θ was varied from 30° to 50° every 5°. The initial decay rate Γ_0 was derived from a first cumulant analysis of the normalized field autocorrelation function. The diffusion coefficient D_0 was estimated from the q^2-dependence $\Gamma_0 = D_0 q^2$, and the hydrodynamic radius R_H obtained via the Stokes-Einstein relation $D_0 = k_B T/(6\pi\eta_s R_H)$, where k_B, η_s, and T are the Boltzmann constant, solvent viscosity, and absolute temperature, respectively.

II. THE CHOICE OF THE DESIGNING FORCE

One of the main aim of this study is to set up a protocol being able to finely control the radial density distribution of the microgel. In the following, we discuss how to implement this feature using a designing force during the self-assembly of the patchy particles mimicking monomers (bivalent) and crosslinkers (tetravalent) in a spherical cavity.

Here we specifically target to reproduce the topology of PNIPAM microgels synthesized using free radical precipitation polymerization. For these particles, the core slowly rarefies from the center towards the corona, resulting in a linearly decreasing density profiles, as observed

[a] crassous@pc.rwth-aachen.de

[b] emanuela.zaccarelli@cnr.it

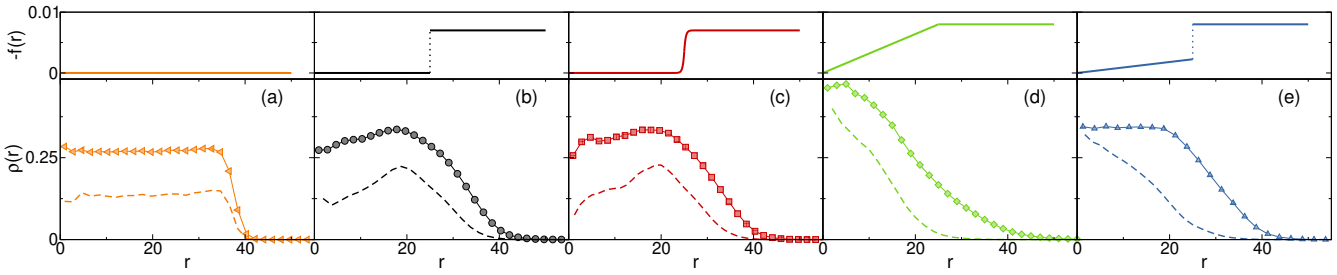

FIG. S1. Forces acting on crosslinkers (top panel) and corresponding density profiles for all particles (symbols) and for crosslinkers only (dashed lines). (a) no force is applied on crosslinkers (b)-(e) different inward forces are considered. The integral of $\rho(r)$ is normalized to a constant value $\int \rho(r)dr = c$ with $c = 10, 5$ respectively for all particles and crosslinkers to improve visualisation. Data are averaged over four independent realizations. Case (e) is the one adopted in the main text.

through super-resolution microscopy [4]. Also the corona should be reproduced with the correct width and shape. In experiments, it was conjectured that the denser core is the result of a faster consumption of the crosslinker with respect to NIPAM [5] during the polymerization process. For this reason, we choose to apply a force acting on crosslinkers only. The exact shape that the force should assume is not *a priori* obvious. In order to obtain the desired density profile, different functional forms of the force were tested. Hereby, we report results that were obtained with four different forces, shown in Fig. S1. We also add the result of the unperturbed case, i.e. assembly in the absence of a force as adopted in Ref. [6]), for comparison. The assembly is carried out by fixing the total number of particles to $N = 42000$ with a fraction of crosslinkers equal to 5%. We confine the system in a spherical cavity of radius Z, which determines the number density and the size of the final microgel. Using too small or too large values of Z gives rise to microgels that are either too compact or too fluffy, very far from the core-corona structure. We thus select the intermediate value of $Z = 50\sigma$, which correspond to a number density $\rho \sim 0.08$, that provides the best conditions to reproduce experiments with the additional force on the crosslinkers. All the configurations are realised using the protocol described in the main text.

In Fig. S1 we report a sketch of the designing force as a function of the distance from the center (top panels) and the associated density profiles (bottom panels) for all the monomers (symbols) and for crosslinkers only (dashed lines).

In the absence of a designing force, shown in Fig S1(a), we find that the microgel is made of a homogeneous core and of a rapidly decaying corona. This is reflected by the flat density profile of the crosslinkers. This effect worsens when we increase the microgel size, giving rise to an unrealistically thin corona. In order to widen the corona, we apply an inward force with spherical symmetry inside the cavity. We use forces of two types. The first type is described by the following expression:

$$\vec{f}_1 = \begin{cases} -kr\hat{r} & \text{if } 0 < r \leq C \\ -g\hat{r} & \text{if } C < r < Z, \end{cases} \tag{1}$$

where $\hat{r}$ is a versor pointing outward. Here an elastic force with a coefficient k acts from the center up to the half radius of the cavity and a gravitational force of constant g is present for larger distances. We choose $C = \frac{Z}{2}$ as the point where the force changes type in order to reproduce a core corona structure for the microgel. We verified that the shape of the resulting microgel is nearly the same for values of this point up to $3Z/5$. The second type of forces smooths out the discontinuity at $Z/2$, increasing continuously from the center to the cavity boundary:

$$\vec{f}_2 = \begin{cases} -\left[\frac{m}{2}\exp\left(\frac{r-C}{t}\right)\right]\hat{r} & \text{if } 0 < r \leq C \\ -\left[m - \frac{m}{2}\exp\left(-\frac{r-C}{t}\right)\right]\hat{r} & \text{if } C < r < Z. \end{cases} \tag{2}$$

Here m, t determine the strength and the smoothness of the force, respectively. We use again $C = \frac{Z}{2}$.

Initially, we consider a force f of type f_1 with gravity constant $g = 8 \times 10^{-3}$ and $k = 0$, shown in Fig. S1(b). One can observe that, although the corona becomes larger, the core is sparser for small r and denser close to the corona. This entails the emergence of a peak at $r \lesssim Z/2$ showing that crosslinkers tend to accumulate towards the center of the microgel, which is not compatible with experimental findings for the class of microgels used in this study. Since the presence of a peak could be due to the discontinuity of f at $Z/2$, we have also employed a force of type f_2 by Eq. 2. We tried multiple values of force parameters, finding that the peak could not be removed. The choice $m = 7 \times 10^{-3}$ and $t = 0.3$ provides a density profile very similar to the previous one (see Fig. S1(c)) for both monomers and crosslinkers. One can then conclude that the additional peak is not given by the discontinuity itself but it has to be a consequence of the weakness or absence of the force in the region $0 < r < Z/2$. Therefore, our next attempt is to maintain the corona shape of the previous examples and get rid of the peak. To this aim, we again employ a force of type f_1 with $g = 8 \times 10^{-}3$ and $k = \frac{2g_1}{Z} = 3.2 \times 10^{-4}$. The use of $k \neq 0$ corresponds to apply an elastic force in the inner half region, Eq. 1 which is continuous at $Z/2$. Furthermore, we employ the same value of g as before in order to keep unchanged the shape of the corona. The

resulting density profile is reported in Fig. S1(d). In this case, we notice that the density distribution inside the microgel is strongly altered, with a continuously decreasing density from the center to the cavity boundary. The absence of a core is totally different from experimental observations.

We infer that this effect is a consequence of the intensity of the force for $r < Z/2$, and therefore we decide to decrease the spring constant of the force as sketched in Fig. S1(e), resulting in a discontinuity at $Z/2$. Using the value $k = 4.5 \times 10^{-5}$, we find a density distribution in the core in agreement with the experiments as discussed in the main text, while preserving the right shape of the corona. Interestingly, in this case, the crosslinker profile is continuously decreasing from the center of the microgel and does not reflect the total profile of all the monomers. This choice is the one adopted in the main text for all system sizes.

III. SIZE AND FORCE EFFECTS ON THE MICROGEL INTERNAL TOPOLOGY

We provide information on the internal topology of the microgels as a function of N by focusing at the chain distribution. A chain is here defined as the sequence of monomers included between two subsequent crosslinkers. The chain length distribution N_l is computed for three sizes of the system assembled in presence of the force and for a large unperturbed system and is reported in Fig. S2. As shown previously [7], the assembly in absence of a designing force leads to a network structure in good agreement with the Flory theory (blue triangles). However, introducing the force an increased number of chains with lengths $l > 50$ can be found. This effect holds even changing the system size, although the probability of having longer chains increases with N. While in the absence of the force, N_l is well described by a single exponential, when the force is introduced we have that the same exponential holds only for relatively short chains, while a second exponential decay describes the large chain distribution. These results confirm that, upon changing N, the internal topology of the network is preserved.

IV. ROBUSTNESS OF α-T RELATIONSHIP WITH RESPECT TO SYSTEM SIZE

To validate the size independence of our model during swelling we compare the experimental form factors with those calculated from simulations of different system sizes using the same α values as reported in the main text for the largest system. We employ the same procedure to rescale the numerical data on the experimental one: we define a conversion factor $\gamma_{5000} = 0.05798$ and $\gamma_{42000} = 0.1245$ to superimpose the experimental and numerical first peak of $P(q)$ respectively for the small (Fig. S3) and the medium (Fig. S4) size systems. These

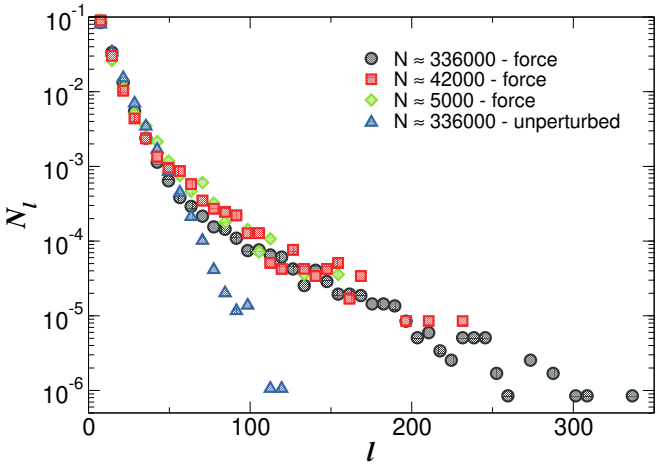

FIG. S2. Chain length distribution N_l for microgels in absence and in presence of the designing force. The former case is reported with blue triangles for a large $N \approx 336000$ system. The latter is shown for three different sizes, a small $N \approx 5000$ system (green diamonds), a medium size $N \approx 42000$ system (red squares), and a large $N \approx 336000$ system (black circles).

two values are used to rescale the q-axis of numerical form factors for all investigated αs. Strikingly, the swelling behavior is well captured using any system size. The peaks are indeed found in the position corresponding to those of the experimental curves, even though they are barely visible, especially for the smallest studied system. The high-q deviations between experiments and simulations become more evident as N decreases, but the agreement improves at high T. We again emphasize how the size independence of our procedure is a confirmation of its reliability in reproducing real world results.

V. DENSITY PROFILES FROM THE STANDARD AND GENERALIZED FUZZY SPHERE MODELS

One of the most successful model to describe microgel density distribution is the widely employed fuzzy sphere model [5], where a microgel is considered as a sphere of radius R' with a homogeneous core followed by a fuzzy corona. Recent results from super-resolution microscopy have shown a slightly inhomogeneous core [4] and put forward a generalization of the fuzzy sphere model with the addition of a linear dependence of the density inside the core. In real space, this model is represented by an error function multiplied by a linear term as shown in Eq.(2) of the main text. In this Equation, we recall that s accounts for the slope of the linear term and, thus, for $s = 0$ the standard fuzzy sphere model is recovered. The generalized fuzzy sphere model of Eq.(2) of the main text

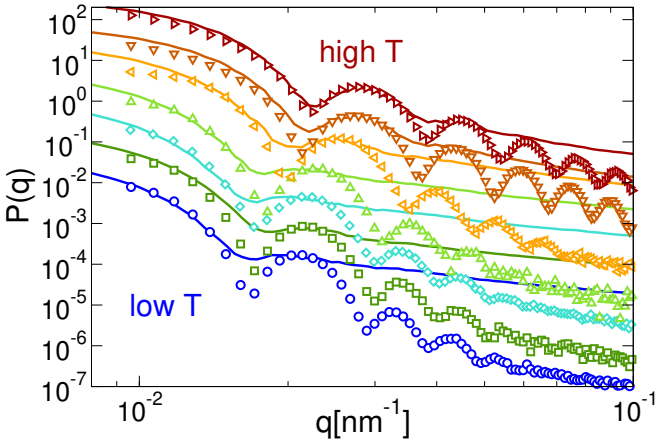

FIG. S3. The form factor for experiments (symbols) and simulations of the system with $N \approx 5000$ (full lines). Data are shifted for clarity and reported with increasing T and α from bottom to top.

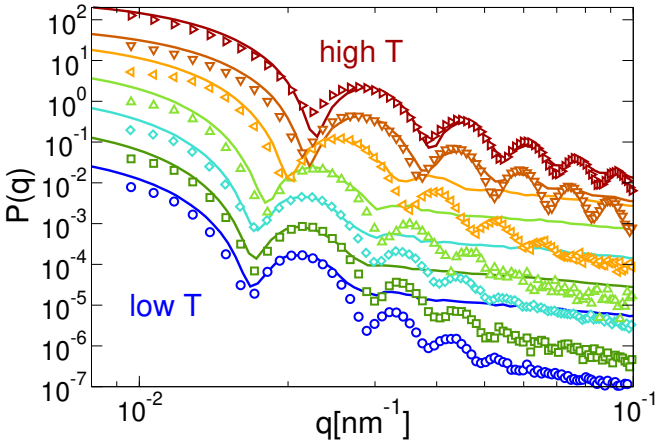

FIG. S4. The form factor for experiments (symbols) and simulations of the system with $N \approx 42000$ (full lines). Data are shifted for clarity and reported with increasing T and α from bottom to top.

can be written in Fourier space as:

$$P(q) \propto \left\{ \left[\frac{3(\sin(qR) - qR\cos(qR))}{(qR)^3} + \right.\right. \\ \left. + s\left(\frac{\cos(qR)}{q^2R} - \frac{2\sin(qR)}{q^3R^2} - \frac{\cos(qR)-1}{q^4R^3} \right) \right] \\ \left. \times \exp\left[-\frac{(\sigma q)^2}{2} \right] \right\}^2 . \quad (3)$$

To compare predictions from the standard and the generalized fuzzy sphere models in real space, we use them to fit the form factors and to extract the associated density profiles. These are compared with those calculated numerically for the largest investigated microgels in Fig. S5. Here, the x-scale has been again rescaled to real units (nm) using the γ factor discussed in the main text. We find that the generalized fuzzy sphere model agrees very well with the numerical data both in the inner part of the core and in the corona. For intermediate values of r there are some small deviations, mainly due to the non-linear decrease of the density profile. On the other hand, the standard fuzzy sphere model shows a weaker agreement with the calculated profile, especially due to the presence of the completely homogeneous core. The disagreement becomes more evident at high T where the standard fuzzy sphere results show a step-like behavior. Instead, a continuously decreasing profile is still observed in simulations and for the generalized fuzzy sphere model, again in close agreement to each other.

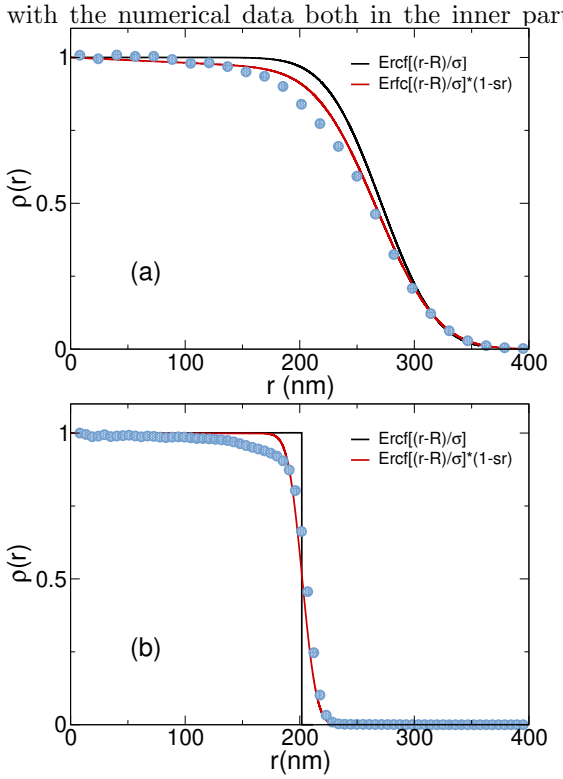

FIG. S5. Comparing density profiles for the standard (black) and generalized (red) fuzzy sphere models with the numerical results (blue symbols) for $T = 15.4°$C (a) and $T = 40.4°$C (b). All data are rescaled to 1 at $x = 0$ for clarity.

[1] D. Paloli, P. S. Mohanty, J. J. Crassous, E. Zaccarelli, and P. Schurtenberger, Soft Matter **9**, 3000 (2013).

[2] P. S. Mohanty, D. Paloli, J. J. Crassous, E. Zaccarelli, and P. Schurtenberger, The Journal of Chemical Physics **140**, 094901 (2014).

[3] I. D. Block and F. Scheffold, Review of Scientific Instruments **81**, 123107 (2010).

[4] S. Bergmann, O. Wrede, T. Huser, and T. Hellweg, Phys-

ical Chemistry Chemical Physics **20**, 5074 (2018).
[5] M. Stieger, W. Richtering, J. S. Pedersen, and P. Lindner, The Journal of Chemical Physics **120**, 6197 (2004).
[6] N. Gnan, L. Rovigatti, M. Bergman, and E. Zaccarelli, Macromolecules **50**, 8777 (2017).
[7] L. Rovigatti, N. Gnan, and E. Zaccarelli, Journal of Physics: Condensed Matter **30**, 044001 (2017).